Preprints.org

Article

Not peer-reviewed version

Application of Cold Sintering Process for Stabilizing Heavy Metals in Municipal Solid Waste Incineration Fly Ash

Shih-Kai Liao , Zhong-En Wu , Yun-Hwei Shen *

Posted Date: 8 August 2023

doi: 10.20944/preprints202308.0203.v2

Keywords: MSWI fly ash; cold sintering process; heavy metal solidification; resource utilization; Taguchi method

Preprints.org is a free multidiscipline platform providing preprint service that is dedicated to making early versions of research outputs permanently available and citable. Preprints posted at Preprints.org appear in Web of Science, Crossref, Google Scholar, Scilit, Europe PMC.

Copyright: This is an open access article distributed under the Creative Commons Attribution License which permits unrestricted use, distribution, and reproduction in any medium, provided the original work is properly cited.

Preprints (www.preprints.org) | NOT PEER-REVIEWED | Posted: 8 August 2023 doi:10.20944/preprints202308.0203.v2

Disclaimer/Publisher's Note: The statements, opinions, and data contained in all publications are solely those of the individual author(s) and contributor(s) and not of MDPI and/or the editor(s). MDPI and/or the editor(s) disclaim responsibility for any injury to people or property resulting from any ideas, methods, instructions, or products referred to in the content.

Article

Application of Cold Sintering Process for Stabilizing Heavy Metals in Municipal Solid Waste Incineration Fly Ash

Shih-Kai Liao, Zhong-En Wu and Yun-Hwei Shen *

Department of Resources Engineering, National Cheng Kung University, Tainan 70101, Taiwan; skyc89@gmail.com (S.-K.L.); peter0010902@gmail.com (Z.-E.W.)

* Correspondence: yhshen@mail.ncku.edu.tw

Abstract: Municipal solid waste incineration fly ash (MSWI FA) predominantly consists of compounds comprising elements such as calcium, aluminum, silicon, sodium, and others. Additionally, it encompasses a complex mixture of heavy metals, chlorides, sulfates, organic pollutants, and other constituents. The effective and economically viable treatment of MSWI FA poses a formidable challenge for the current stage of resource cycling. In this research report, we will adopt a novel low-temperature sintering method called "Cold Sintering Process" (CSP) as a means to immobilize heavy metals within the fly ash. By utilizing a Taguchi orthogonal array, we will adjust five control factors in the CSP, including sintering temperature, uniaxial pressure, sintering time, initial water addition, and sodium carbonate dosage. The leaching of cadmium element from the fly ash, as measured by TCLP, will serve as the quality indicator. Through the application of CSP, the MSWI FA will be transformed into structurally stable ceramic blocks, effectively immobilizing the heavy metals within the blocks. The results of the experiments showed that MSWI FA under the conditions of a temperature of 300°C, uniaxial pressure of 312 MPa, sintering time in 60 minutes, 25 wt% water addition, and 9 wt% Na_2CO_3 addition could effectively reduce the leaching of cadmium by 77.71%, lead by 21.14%, zinc by 42.37%, and chromium by 99.99%, as compared to the original MSWI FA TCLP results.

Keywords: MSWI fly ash; cold sintering process; heavy metal solidification; resource utilization; Taguchi method

1. Introduction

The Incineration is currently considered as one of the effective approaches for urban waste management [1]. By subjecting municipal solid waste (MSW) to the incineration process, a substantial reduction in volume can be achieved, accompanied by the recovery of energy for electricity generation [2], thereby addressing various challenges associated with waste landfilling. Following incineration, the overall waste volume is reduced by 85% to 90%, with a corresponding decrease in mass ranging from 60% to 90%[3]. Additionally, the process generates approximately 15% to 20% of bottom ash (BA) and 3% to 5% of fly ash (FA)[4]. The subsequent management and resource circulation of fly ash residues are significant concerns to be addressed.

The main constituents of municipal solid waste incineration fly ash (MSWI FA) are compounds composed of Ca, Si, Al, Cl, Na, K, S, Fe, Mg, P, among others. Trace elements (<1%) include heavy metal compounds such as Pb, Zn, Cd, Cu, Hg, Cr, Ni, As, and others[3]. The particles of fly ash exhibit irregular shapes, with sizes predominantly ranging from <10 μm to 50 μm[5]. The source of heavy metals in fly ash is the waste itself, and they become associated with the fly ash during the incineration process through the following mechanisms: (1) Volatile forms of heavy metal compounds are released during combustion. (2) These volatiles undergo chemical reactions and become enriched on the surface of the fly ash. (3) The flue gas, along with the particles, enters the air pollution control system. (4) The particles are captured by the air pollution control system[3, 5-7].

© 2023 by the author(s). Distributed under a Creative Commons CC BY license.

Preprints (www.preprints.org) | NOT PEER-REVIEWED | Posted: 8 August 2023 doi:10.20944/preprints202308.0203.v2

In recent years, research on fly ash treatment can be broadly categorized into three aspects: thermal treatment[8, 9], stabilization/solidification (S/S)[10, 11], and chemical separation[5, 12-14]. Thermal treatment and S/S primarily aim to promote overall structural stability through the generation of secondary phases or physical encapsulation, thereby reducing the mobility of internal contaminants[10, 15]. Chemical separation, on the other hand, focuses on the separation of target elements using hydrometallurgy techniques[16-18]. In 2016, Randall and his research team introduced a novel sintering technique called the Cold Sintering Process (CSP). This technique requires a temperature below 350°C, along with the application of uniaxial pressure and pre-wetting of ceramic powders. Remarkably, within a span of 2 hours, highly dense ceramic blocks can be obtained through this method[19-22].

However, most studies have focused on utilizing CSP to enhance the electrical properties of ceramic materials by modifying experimental parameters such as sintering time, uniaxial stress, sintering time, and liquid additives[23-25]. In this research, our team aims to apply the CSP technique to treat MSWI FA from Taiwan. Initially, the FA powder undergoes pre-treatment through drying, ball milling, and sieving. Subsequently, the fly ash powder is subjected to CSP experiments based on a Taguchi orthogonal array ($L_{16}(4^5)$), where it is sintered into ceramic blocks. The TCLP (Toxicity Characteristic Leaching Procedure) test is conducted for 18 hours to evaluate the leaching of cadmium metal in the fly ash. The leaching amount of cadmium metal in the TCLP test serves as the basis for adjusting the control factor parameters to determine the optimal combination for immobilizing heavy metals within the fly ash. Additionally, XRD (X-ray Diffraction) and SEM-EDS (Scanning Electron Microscopy-Energy Dispersive X-ray Spectroscopy) analysis are employed to further investigate the solidification mechanism.

2. Materials and Methods

2.1. MSWI Fly ash

The MSWI fly ash utilized in this research was sourced from an incineration facility located in southern Taiwan. To ensure sample homogeneity, grab samples were collected from the bag filter and subsequently mixed in a laboratory blender for 30 seconds. The coning and quartering method was employed to reduce the sample weight to 2 kg while maintaining representativeness. Subsequently, the fly ash samples were sieved, and the fraction with a diameter smaller than 0.59 mm was collected for use in the subsequent experimental procedures. Preliminary analysis of the fly ash was conducted using XRF to determine the elemental composition and approximate proportions within the ash. Simultaneously, three sets of fly ash samples, each weighing 0.4 g, were subjected to complete digestion using aqua regia under the conditions of L/S ratio of 50, temperature of 200°C, and a dwell time of 120 minutes. Following digestion, the resulting solution was analyzed for its elemental composition using flame atomic absorption spectroscopy (AAS). The XRF analyses and aqua regia digestion experiments were conducted repeatedly to compare and determine the relative weight percentages of elements within the fly ash. This comparative analysis enabled us to ascertain the respective contributions of each element in the fly ash composition. The fly ash samples underwent an analysis of their crystalline phase composition using XRD. Surface morphology and initial particle size analysis of the fly ash samples were conducted using SEM after coating the samples with Au. Moreover, the SEM observations were complemented by laser particle size analysis to obtain a comprehensive characterization of the particle size distribution in the fly ash samples.

2.2. CSP Pre-treatment

The main purpose of the CSP pretreatment is to eliminate impurities and oversized aggregates from the fly ash samples, while simultaneously reducing the particle size and narrowing the overall particle size distribution. This pre-treatment process is crucial for facilitating the densification process during CSP, enabling effective compaction and enhancing the overall performance of the material. The pretreatment procedure began with the placement of the fly ash in an oven at 70°C for 24 hours, aiming to remove any residual moisture present in the samples. Subsequently, the fly ash underwent

Preprints (www.preprints.org) | NOT PEER-REVIEWED | Posted: 8 August 2023 doi:10.20944/preprints202308.0203.v2

a 24-hour ball milling process to reduce its particle size. To eliminate oversized impurities and agglomerates, the pretreated fly ash was subjected to sieving using 10 mesh (about 1700 microns) and 150 mesh (about 106 microns) screens. These meticulous pretreatment steps were implemented to ensure the effective removal of excess moisture, achieve finer particle size, and eliminate larger impurities and agglomerates from the fly ash samples, ultimately enhancing the quality and suitability of the material for subsequent processing.

2.3. Cold Sintering Process

In this study, we selected five control factors based on relevant literature that may affect the quality of CSP. These factors include A: Sintering temperature, B: Magnitude of uniaxial pressure, C: Sintering time, D: Initial water addition, and E: Fly ash + sodium carbonate addition. The CSP experiments were conducted by gradually heating at a rate of 10°C per minute while keeping the other factors constant. Before conducting the CSP experiments, the pre-treated fly ash and sodium carbonate were meticulously blended according to the prescribed experimental proportions. The resulting powder mixture was uniformly wetted with the addition of water and vigorously stirred to achieve homogeneity. The specific procedure for the preparation is illustrated in Figure 1. The prepared CSP slurry from Figure 1. was poured into the mold shown in Figure 2-b, which has an inner diameter of 2 cm.

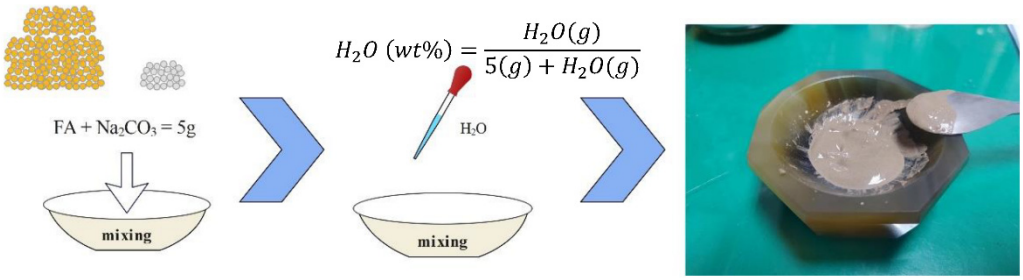

Figure 1. Steps for Fly Ash CSP Material Preparation.

The CSP equipment used in this study was custom-designed and assembled, as shown in Figure 2. The mold had an inner diameter of 20 mm and could withstand a maximum uniaxial pressure of 15 tons. The mold heater was capable of ramping up the temperature at a rate of 10 °C per minute and heating up to a maximum temperature of 320°C.

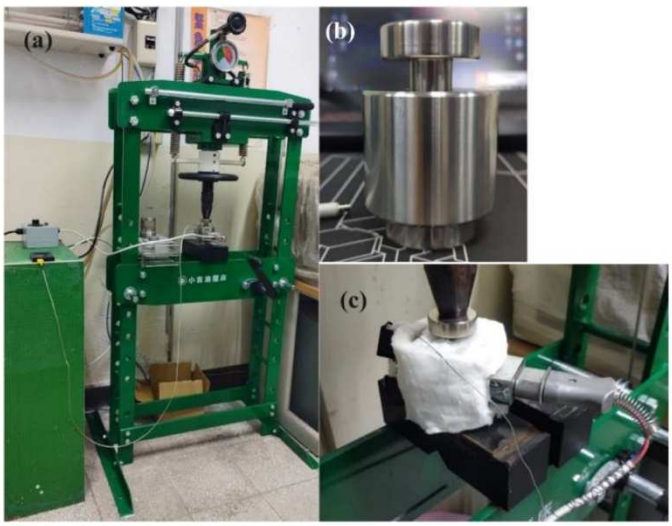

Note: (a) The temperature control system is depicted on the left side of the diagram, connected to the central mold heater for heating the mold. (c) During actual CSP process, an additional layer of white insulation cotton is added around the mold heater to minimize the impact of room temperature during the heating stage.

Figure 2. CSP Experimental Setup: (a) Overall view of the CSP equipment. (b) Customized mold used for CSP. (c) Mold heater.

Preprints (www.preprints.org) | NOT PEER-REVIEWED | Posted: 8 August 2023 doi:10.20944/preprints202308.0203.v2

During the CSP process, it can be divided into two stages: stage 1 and stage 2. In stage 1, only uniaxial pressure is applied. At this stage, the uniaxial pressure promotes further reactions between the fly ash particles and the pre-added water. Some substances in the fly ash, such as soluble salts and certain heavy metals, also undergo a transfer to the liquid phase during this stage. The dissolution of fly ash particles in terms of quantity significantly affects the densification of the subsequent CSP product. Additionally, under the influence of uniaxial pressure, some fly ash particles undergo plastic deformation, and the stacking of fly ash particles becomes denser compared to when no uniaxial pressure is applied. Upon reaching the specified pressure, stage 2, also known as the heating stage, commences. In this stage, the interplay of temperature, pressure, and water induces the release of more internal constituents from the fly ash particles into the water. As the temperature surpasses the boiling point of water, evaporation occurs. The originally dissolved substances in the water become supersaturated, precipitating onto the surface of primary-phase fly ash particles and forming secondary phases. This dissolution-precipitation reaction continues to take place iteratively during stage 2. Finally, with the combined effect of temperature and pressure, all solvents evaporate, resulting in the formation of densely consolidated fly ash blocks.

2.4. Taguchi method parameter optimization

In the absence of sufficient data in the existing literature on CSP for fly ash, we relied on the definitions, technical specifications, and constraints mentioned in current CSP literature[23-25]. Additionally, we considered and referenced similar stabilization techniques applied to fly ash at its current stage, such as Hydrothermal Reaction Sintering[26, 27], Cold Sintering[28, 29], Hydrothermal Hot Pressing[23, 30], and Reactive Hydrothermal Liquid-Phase Densification[31]. Based on this information, we selected five key control factors and their corresponding levels that have the most significant impact on heavy metal immobilization in CSP for fly ash. To explore the effects of each factor on heavy metal immobilization, we employed the Taguchi method, which allowed us to predict the optimal experimental conditions. By combining the knowledge from existing CSP literature and analogous techniques, we aimed to bridge the knowledge gap and establish a framework for conducting CSP experiments on fly ash, specifically focusing on its ability to immobilize heavy metals.

In this study, the $L_{16}(4^5)$ orthogonal array was employed as the experimental basis for discussing the results of the CSP experiments. The control factors investigated include A: Sintering temperature, B: Uniaxial pressure, C: Sintering time, D: Water addition, and E: Sodium carbonate addition. Each control factor consists of four levels, as shown in Table 2. After undergoing CSP, the fly ash is transformed into a solidified form. To effectively describe the leaching behavior of heavy metals in fly ash CSP blocks, it is necessary to select one specific heavy metal as the leaching indicator. Common heavy metals found in fly ash, such as Zn, Pb, Hg, Cu, Cr, Cd, and Ni, are all viable choices. Among these heavy metals, Cd [5]and Pb[32] are considered the least stable and are more susceptible to environmental influences, potentially contaminating groundwater. However, due to the amphoteric property, Pb undergoes dissolution-precipitation-secondary phase formation processes during CSP, which can introduce larger uncertainties and errors. Therefore, Cd was ultimately selected as the quality characteristic for the Taguchi experimental design in order to assess the leaching behavior of heavy metals in fly ash CSP blocks. To analyze the data, several techniques were employed, such as calculating the signal-to-noise (S/N) ratio, determining the factor effects, plotting factor effect charts, and adjusting the factor levels to maximize the S/N ratio. Through these approaches, an empirical model was established, and the optimal theoretical experimental parameters for enhancing the heavy metal immobilization capacity in CSP were determined. Additionally, validation experiments were conducted to compare the calculated values with the actual experimental results and explore potential reasons for any discrepancies observed.

Preprints (www.preprints.org) | NOT PEER-REVIEWED | Posted: 8 August 2023 doi:10.20944/preprints202308.0203.v2

Table 1. $L_{16}(4^5)$ 4-levels orthogonal array.

	A	B	C	D	E
EXP.	sintering temperature	uniaxial pressure	sintering time	water additives	Na_2CO_3 additives
1	1	1	1	1	1
2	1	2	2	2	2
3	1	3	3	3	3
4	1	4	4	4	4
5	2	1	2	3	4
6	2	2	1	4	3
7	2	3	3	1	2
8	2	4	4	2	1
9	3	1	3	4	2
10	3	2	4	3	1
11	3	3	1	2	4
12	3	4	2	1	3
13	4	1	4	2	3
14	4	2	3	1	4
15	4	3	2	4	1
16	4	4	1	3	2

Table 2. Different levels of the control factors in the $L_{16}(4^5)$ orthogonal array.

	sintering temperature	**uniaxial pressure**	**sintering time**	**water additives**	**Na_2CO_3 additives**
Level 1	150 ℃	7.5 T (234MPa)	30 mins	10 wt%	3 wt%
Level 2	200 ℃	10 T (312MPa)	60 mins	15 wt%	5 wt%
Level 3	250 ℃	12.5 T (390MPa)	90 mins	20 wt%	7 wt%
Level 4	300 ℃	15 T (468MPa)	120 mins	25 wt%	9 wt%

3. Results and Disscusssion

3.1. Characteristics of Fly Ashes

The fly ash used in this study, derived from municipal solid waste (MSW), was obtained from the Chengxi Incineration Plant situated in Tainan, Taiwan. The initial phase of the experimental investigation involved a comprehensive analysis aimed at determining the intrinsic properties of the fly ash. Utilizing the X-ray fluorescence (XRF) technique, an elemental analysis was performed, and the obtained results are presented in Table 3. Subsequently, aqua regia digestion was conducted on the fly ash, followed by elemental analysis using atomic absorption spectrometry (AAS). Table 4. provides an overview of the relative proportions of different elements identified in the fly ash. Comparative analysis of Table 3. and Table 4. reveals that the dominant constituents of the fly ash primarily consist of calcium, sodium, and potassium, whereas the proportions of heavy metals, such as zinc, lead, copper, chromium, and cadmium, are comparatively lower. Despite the relatively low concentrations of heavy metals in the fly ash, their potential for leaching remains a significant environmental concern.

Preprints (www.preprints.org) | NOT PEER-REVIEWED | Posted: 8 August 2023 doi:10.20944/preprints202308.0203.v2

The XRD analysis conducted on the fly ash sample at room temperature, as illustrated in Figure 1., revealed the predominant crystalline phases present in the fly ash composition. These include NaCl (Halite, PDF#05-0628), SiO_2 (Quartz, PDF#46-1045), $CaCO_3$ (Calcite, PDF#05-0586), $CaSO_4$ (Anhydrite, PDF#37-1496), and KCl (Sylvite, PDF#41-1476). Based on the X-ray diffraction (XRD) results, it can be observed that the fly ash used in this study exhibits minimal differences compared to fly ash generated from general municipal waste incineration.

SEM images at different magnifications, as illustrated in Figure 4.(a) and 4.(b), depict the surface morphology of fly ash particles in their original state. Figure 4.(a) displays the SEM image of the fly ash sample at 800 times magnification, revealing conglomerates of larger fly ash particles composed of numerous smaller particles with sizes ranging approximately in the tens of micrometers. These larger particles exhibit a multi-layered structure, indicative of agglomerates rather than individual primary particles. The loose stacking of these large particles suggests a lack of strong bonding between them. The irregular surface topography of these particles results from their formation through the gradual aggregation of acidic high-temperature flue gas (containing heavy metals, organic compounds, etc.) generated during waste incineration, followed by the introduction of alkaline agents in the gas treatment system.

Increasing the SEM magnification to 8000 times in Figure 4.(b) allows for clear visibility of the smaller fly ash particles on the surface of the larger particles. These smaller particles exhibit sizes ranging from approximately 1 to 10 micrometers and possess a more angular and disordered shape. Previous studies have reported a typical particle size range of 10-50 micrometers for fly ash, although larger fly ash particles up to 300 micrometers in size have been observed. The results of laser particle size analysis conducted on the fly ash samples are presented in Figure 5. The D50 value, representing the median particle size, is determined to be 8.24 micrometers. The particle size distribution of the fly ash sample ranges from approximately 0.67 micrometers to 34.57 micrometers, as depicted in the graph. These findings align with the observations from the SEM analysis in Figure 2, providing further evidence of a diverse range of particle sizes present in the fly ash sample.

Table 3. MSWI fly ash XRF composition analysis results.

Elements	Ca	Na	K	Zn	Pb	Cu	Cr	Cd
wt%	58.39	21.35	10.71	6.23	2.59	0.51	0.15	0.06

Table 4. Analysis results of fly ash digestion in aqua regia solution.

Elements	Ca	Na	K	Zn	Pb	Cu	Cr	Cd
AAS value (mg/L)	2925.958	1052.503	539.745	275.27	101.952	20.075	9.614	3.597
Ratio between elements (wt%)	59.37%	21.35%	10.95%	5.59%	2.07%	0.41%	0.20%	0.07%

Preprints (www.preprints.org) | NOT PEER-REVIEWED | Posted: 8 August 2023 doi:10.20944/preprints202308.0203.v2

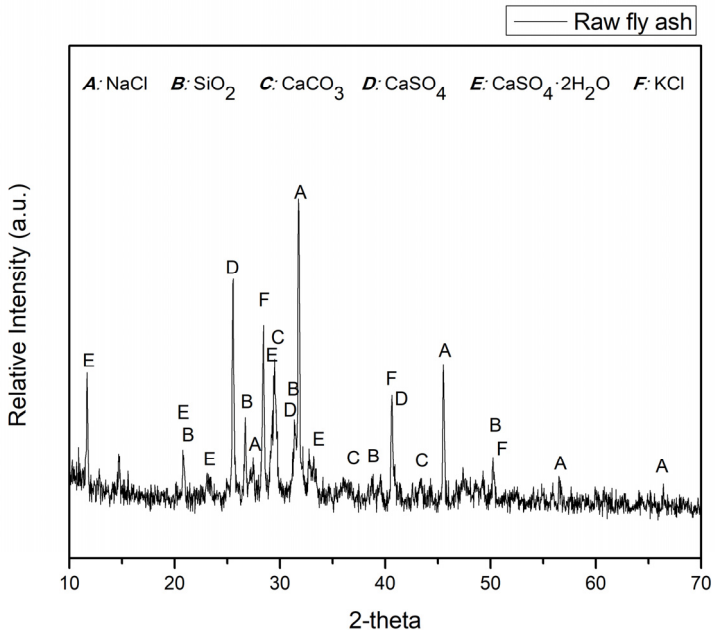

Figure 3. XRD analysis of MSWI fly ash sample.

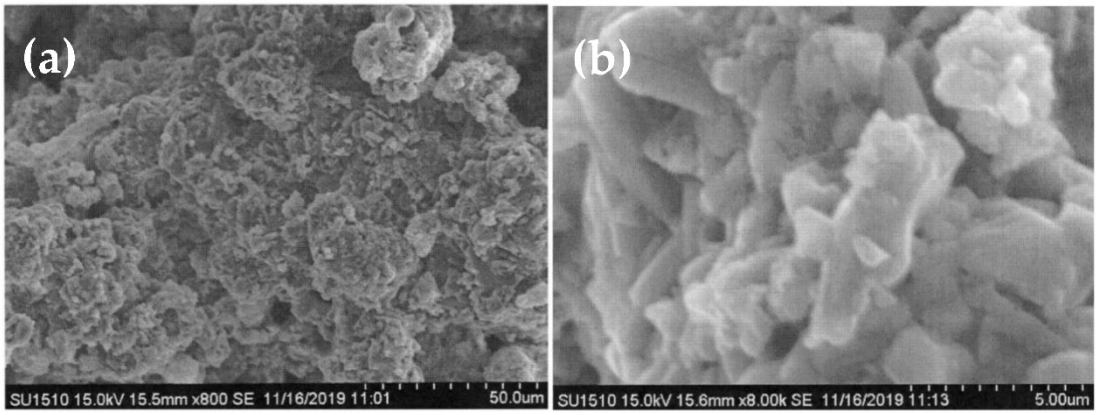

Figure 4. SEM analysis of MSWI fly ash samples (a) 800x (b) 8,000x.

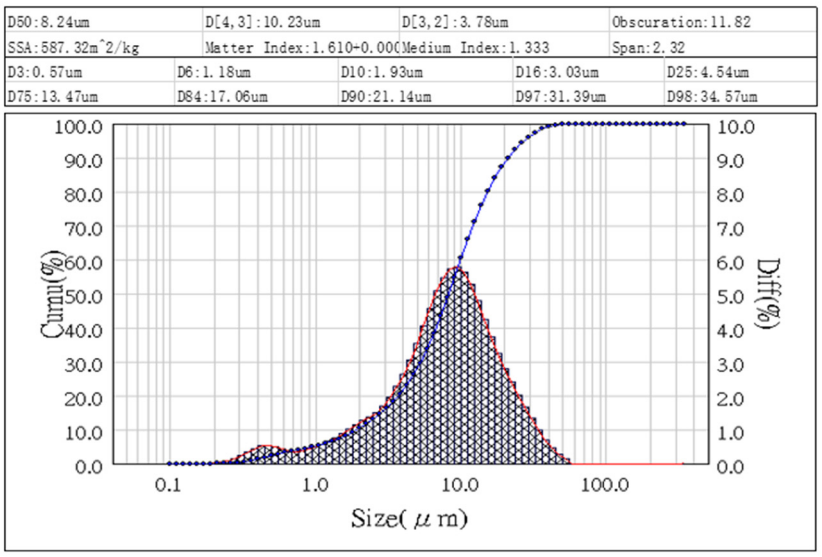

Figure 5. laser particle size analysis of fly ash samples.

Preprints (www.preprints.org) | NOT PEER-REVIEWED | Posted: 8 August 2023 doi:10.20944/preprints202308.0203.v2

3.2. Cold Sintering Process Pre-treatment

In order to enhance the energy efficiency of cold sintering and promote the uniformity of fly ash, a pre-processing step was employed in this study. The fly ash powder underwent a series of treatments, including a 24-hour drying process, a 24-hour ball milling process, and a two-stage sieving process using 50 mesh and 150 mesh screens. The pre-treatment fly ash samples were then subjected to laser particle size analysis and SEM analysis.

Oversized fly ash particles require more energy for densification during the sintering process. Conversely, undersized fly ash particles are prone to move into the gaps between molds during cold sintering, leading to a shortened mold lifespan. In cases where the particle size distribution curve exhibits a bimodal distribution, smaller particles can fill the voids between larger particles, facilitating subsequent densification processes. The particle size distribution analysis, as presented in Figure 7, indicates a notable reduction in the D50 value from 8.24 micrometers to 4.31 micrometers after the pre-processing steps, representing a decrease of 47.7%. Moreover, the particle size distribution range narrowed from 0.67-34.57 micrometers in the original fly ash sample to 0.31-16.25 micrometers after the pre-processing. SEM images Figure 6.(a) and 6.(b) at a magnification of 10,000 times and 30,000 times demonstrate well-defined grain morphology and grain boundaries in the pre-treatment fly ash samples. Notably, the grain edges appear smoother and exhibit reduced angularity compared to the fly ash samples without pre-processing. The sequential treatments of drying, ball milling, and sieving have effectively refined the particle size distribution of the fly ash, resulting in smaller and more uniform particles.

The SEM analysis further verifies the improved surface characteristics of the pre-treatment fly ash, suggesting its potential for enhanced performance in various applications. The optimized particle size distribution and refined morphology attained through the pre-processing steps offer promising prospects for the utilization of fly ash in diverse fields.

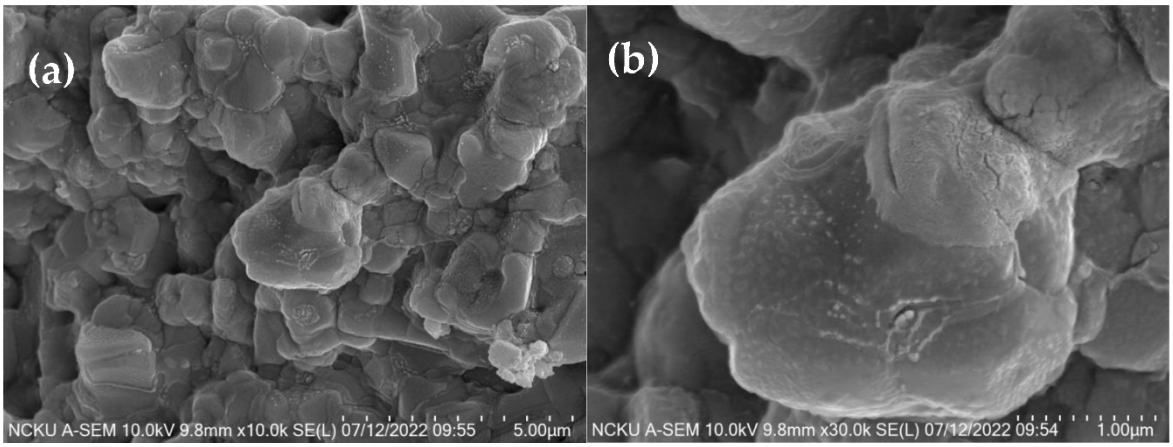

Figure 6. SEM analysis of MSWI fly ash samples after CSP pre-treatment (a) 10,000x (b) 30,000x.

Preprints (www.preprints.org) | NOT PEER-REVIEWED | Posted: 8 August 2023 doi:10.20944/preprints202308.0203.v2

D50:4.31um	D[4,3]:5.31um	D[3,2]:1.78um	Obscuration:12.60	
SSA:1241.84m^2/kg	Matter Index:1.610+0.000	Medium Index:1.333	Span:2.52	
D3:0.37um	D6:0.47um	D10:0.59um	D16:1.06um	D25:1.69um
D75:7.99um	D84:9.79um	D90:11.46um	D97:15.09um	D98:16.25um

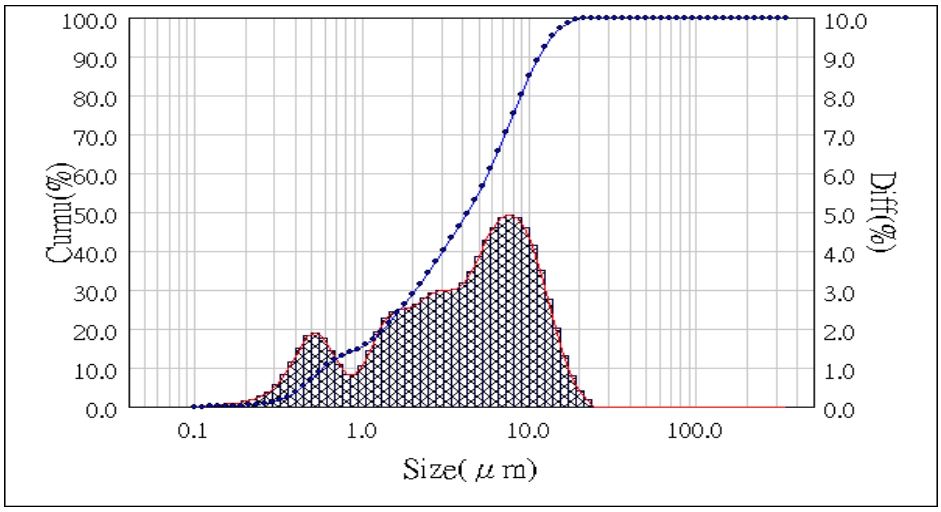

Figure 7. laser particle size analysis results of pre-treated samples.

3.3. Taguchi Experiment and Optimization of Cold Sintering Process

In this study, we employed an $L_{16}(4^5)$ Taguchi orthogonal array to investigate the effects of five control factors, namely sintering temperature, uniaxial pressure, sintering time, water additives, and sodium carbonate additives, on the immobilization of heavy metals during the CSP. The objective was to determine the optimal conditions for effective immobilization of heavy metals in the CSP. Table 1. presents the $L_{16}(4^5)$ Taguchi orthogonal array used in the experimental design, while Table 2. displays the levels of the control factors within the orthogonal array.

The complete results of the $L_{16}(4^5)$ orthogonal array experiment are revealed in Table 5. The first column, labeled EXP., represents the experiment numbers, comprising 16 sets of different combinations of factor levels. Cd(1), Cd(2), and Cd(3) represent the cadmium concentrations (mg/L) measured in the TCLP solution after the fly ash underwent CSP under specific control factor conditions. The number in parentheses denotes the replicate experiment number. The concentration of cadmium in the solution serves as the quality characteristic, indicating the extent of cadmium leaching and serving as an indicator of the effectiveness of heavy metal immobilization. The Cd AVE. represents the arithmetic average of Cd(1), Cd(2), and Cd(3), and it will be utilized in the subsequent calculations of the factor response table/graph. The symbol S_n represents the standard deviation of Cd(1), Cd(2), Cd(3), and Cd AVE., which is calculated using equation (1). In this equation, y_i represents the quality characteristic, $\bar{y}$ represents the average value of the quality characteristic, and n represents the number of individual elements. Unlike the typical formula for standard deviation calculation, equation (1) uses n as the denominator instead of the more common n-1. Under this condition, the sample standard deviation tends to be equal to the population standard deviation. However, regardless of the specific calculation method, the standard deviation represents the degree of dispersion of n data points.

$$S_n = \sqrt{\frac{\sum_{i=1}^{n}(y_i - \bar{y})}{n}} \quad (1)$$

In the Taguchi method, the S/N ratio serves as a quality index, where a higher S/N ratio indicates better quality. In this study, the objective is to minimize the leaching of heavy metals during the TCLP testing, thus adopting the "smaller the better" characteristic for ideal functionality. The S/N ratio calculation for the "smaller the better" characteristic is expressed by equation (2), where $\bar{y}$ represents the mean value and S_n represents the standard deviation.

Preprints (www.preprints.org) | NOT PEER-REVIEWED | Posted: 8 August 2023 doi:10.20944/preprints202308.0203.v2

$$S/N = -10\log(\bar{y}^2 + {S_n}^2) \quad (2)$$

Table 5. Experimental results of FA CSP using $L_{16}(4^5)$ orthogonal array.

EXP.	Cd (1)	Cd (2)	Cd (3)	Cd AVE.	S_n	S/N ratio
1	1.793	1.859	1.892	1.848	0.050	-5.337
2	1.595	1.617	1.54	1.584	0.040	-3.998
3	1.595	1.364	1.375	1.444	0.130	-3.231
4	1.276	1.254	1.166	1.232	0.058	-1.822
5	1.056	1.078	1.056	1.063	0.013	-0.534
6	1.199	1.188	1.243	1.21	0.029	-1.658
7	1.54	1.683	1.463	1.562	0.112	-3.896
8	1.551	1.639	1.881	1.690	0.171	-4.604
9	1.232	1.1	1.298	1.21	0.101	-1.686
10	1.298	1.397	1.298	1.331	0.057	-2.492
11	1.056	1.012	1.122	1.063	0.055	-0.545
12	1.078	1.155	1.056	1.096	0.052	-0.809
13	1.023	1.078	0.902	1.001	0.090	-0.044
14	0.814	1.045	0.814	0.891	0.133	0.906
15	1.045	1.045	0.792	0.961	0.146	0.249
16	1.078	1.023	0.902	1.001	0.090	-0.044
	AVE.			**1.262**	**0.083**	**-1.846**

Cd(1)、Cd(2)、Cd(3)、Cd AVE. are quality characteristic, unit: mg/L. S_n is standard deviation.

Table 6. presents the factor response table of the orthogonal array experiment, while Figure 8 displays the factor response graph. The values in Table 6. represent the S/N ratio contributions of each control factor at different levels, calculated based on the data from Table 1. and Table 5. By recording the S/N ratio contributions of each control factor at different levels, the S/N ratio factor response graph can be plotted. Additionally, by subtracting the maximum and minimum values of the S/N ratio contributions for each control factor at different levels, the Range values in Table 6. are obtained. These Range values indicate the ranking of the impact of each control factor on the S/N ratio.

Table 6. and Figure 8. results indicate the ranking of the impact of control factors on the S/N ratio from highest to lowest as follows: sintering temperature, Na_2CO_3 additives, water additives, sintering time, and uniaxial pressure. Table 7. presents the variability analysis of the experimental results from Table 5.

Table 7. in the context of analysis of variance (ANOVA), SS (Sum of Squares) represents the sum of squared differences between each variation vector and the mean. The Total Sum of Squares (SS_T) is defined as follows:

$$SS_{Tot} = \sum_{i=1}^{n}\sum_{j=1}^{r} y_{ij}^2 - (n \times r \times \bar{y}^2) = SUMSQ(y_{ij} - \bar{y}) \quad (3)$$

Preprints (www.preprints.org) | NOT PEER-REVIEWED | Posted: 8 August 2023 doi:10.20944/preprints202308.0203.v2

Where n is the number of columns in the orthogonal array and r is the number of experimental replications. The sum of squares for the factor effects (SS_A) can be expressed as:

$$SS_A = \frac{n \times r}{L_A} \sum_{k=1}^{L_A} (y_{Ak} - \bar{y})^2 = n \times r \times VARP(\overline{y_{A1}} + \overline{y_{A2}} + \cdots + \overline{y_{L_A}}) \quad (4)$$

Where L_A is the levels of control factor. The sum of squares for error (SS_e) can be expressed as:

$$SS_e = \sum_{i=1}^{n} S_i^2 \times (r - 1) \quad (5)$$

The definition of degrees of freedom (DOF) is that for a set of x samples, when x independent pieces of information can be provided, DOF = x - 1. The total degrees of freedom (DOF_T) can be expressed as:

$$DOF_{Tot} = n \times r - 1 \quad (6)$$

The degrees of freedom for factor A (DOF_A) can be expressed as:

$$DOF_A = L_A - 1 \quad (7)$$

The degrees of freedom for error (DOF_e) can be expressed as:

$$DOF_e = n \times (r - 1) \quad (8)$$

Variance is defined as the SS) divided by the DOF. Taking the square root of this value yields the standard deviation. The relationship between these three measures can be summarized as follows:

$$VAR = \frac{SS}{DOF} = S^2 \quad (9)$$

When the number of sample approaches infinity, the F-value tends to approach 1. In finite samples, a larger F-value indicates that the numerator and denominator come from a smaller probability space within the sample, indicating a stronger impact of the factor effect. In practice, the F-value can be calculated as:

$$F = \frac{mS_Z^2}{S_y^2} = (\frac{SS_A}{DOF_A})/V_{Tot} \quad (10)$$

The denominator (S_y^2) represents the total variance ($V_T = S_T^2$) calculated from the original sample. The numerator (S_Z^2) is the variance estimated from the "sample means" and multiplied by the factor m, resulting in the unaveraged original sample variance. By calculating the magnitude of the F-value, we can make preliminary judgments about the size of the effect of the factor. Furthermore, using a probability function, we can calculate the probability of obtaining an F-value greater than the observed F-value. The calculation can be done as follows:

$$Probability = FDIST(F, DOF_Z, DOF_y) \quad (11)$$

DOF_z represents the degrees of freedom for the numerator in the F-value calculation. It is equal to the total number of sample (n) divided by the factor m, minus 1. DOF_y represents the degrees of freedom for the denominator in the F-value calculation.

Its purpose is to validate the correctness of the ranking of control factor impacts in the S/N factor response table/graph and to examine the significance of control factors in immobilizing heavy metals (whether they have a significant impact or not). The results of the variability analysis in Table 7. confirm that the ranking of control factor impacts in Table 6. and Figure 8. is correct. Furthermore, by maximizing the S/N ratio, the optimal conditions for fly ash CSP in immobilizing heavy metals can be predicted as follows: sintering temperature: level 4 (300°C), uniaxial pressure: level 2 (10 tons), sintering time: level 2 (60 minutes), water additives: level 4 (25 wt%), Na_2CO_3 additives: level 4 (9 wt%). Additionally, an Additive Model can be utilized to calculate the S/N ratio and theoretical values of the quality characteristic for the optimal CSP conditions. A comparison can then be made between the calculated values and the actual experimental data.

Preprints (www.preprints.org) | NOT PEER-REVIEWED | Posted: 8 August 2023 doi:10.20944/preprints202308.0203.v2

Table 6. S/N ratio factor response table.

Cd	sintering temperature	uniaxial pressure	sintering time	water additives	Na_2CO_3 additives
Level 1	-3.597	-1.900	-1.896	-2.284	-3.046
Level 2	-2.673	-1.810	-1.273	-2.298	-2.406
Level 3	-1.383	-1.856	-1.976	-1.575	-1.435
Level 4	0.267	-1.819	-2.240	-1.229	-0.499
Range	3.864	0.090	0.967	1.069	2.547
Rank	1	5	4	3	2

Unit of S/N ratio: dB.

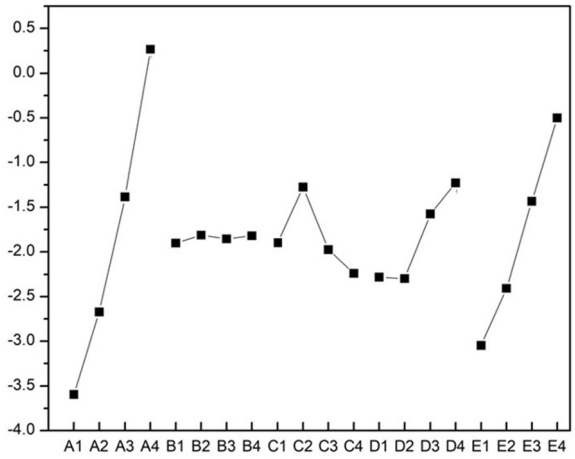

Figure 8. S/N ratio factor response graphic.

Table 7. Analysis of variance results for $L_{16}(4^5)$ orthogonal array experiment.

FACTOR	SS	DOF	Var	F	Probability	Confidence level	Rank/ Significant*?
sintering temperature	2.175	3	0.725	8.538	0.152%	99.85%	1 / Y
uniaxial pressure	0.006	3	0.002	0.023	99.522%	0.48%	5 / N
sintering time	0.127	3	0.042	0.500	68.807%	31.19%	4 / N
water additives	0.329	3	0.110	1.293	31.305%	68.70%	3 / N
Na_2CO_3 additives	1.074	3	0.358	4.215	2.383%	97.62%	2 / Y
Error	0.283	32	0.0089	*At least 97% confidence			
TOTAL	3.992	47	0.085	S=0.094			

After identifying the optimal conditions for CSP in immobilizing heavy metals using the Taguchi method, it is necessary to conduct confirmation experiments. These experiments involve comparing the actual experimental values obtained under the optimal CSP conditions with the theoretical values calculated using the additive model. This comparison aims to assess the accuracy and reliability of the empirical model in predicting the response variable. Table 8 presents a comparison between the additive model calculated values and the average experimental values obtained from triple

Preprints (www.preprints.org) | NOT PEER-REVIEWED | Posted: 8 August 2023 doi:10.20944/preprints202308.0203.v2

replications under the optimal CSP conditions for both the quality characteristic and the S/N ratio. In terms of the quality characteristic, which represents the cadmium leaching concentration of the CSP-treated fly ash blocks after 18 hours of TCLP testing, there is a difference of 0.085 mg/L between the experimental values and the additive model calculated values. For the S/N ratio, there is a difference of 0.615 dB. The slight differences between the additive model theoretical values and the experimental values can be attributed to several possible reasons identified by our team. Firstly, it is possible that certain control factors with significant effects were overlooked during the initial selection process. For example, the inclusion of more effective solid additives or solution additives that facilitate the CSP process might have improved the results. Secondly, there may be interactions among the existing control factors that were not accounted for, leading to deviations in the predictions of the empirical model. Finally, there could be noise factors present in the experimental conditions of the existing control factors that cannot be ignored, contributing to the observed discrepancies.

Based on the results from the factor response graphs/tables and the variance analysis, it can be observed that under the current selection of control factors and their respective levels, the optimal CSP conditions (sintering temperature: 300°C, uniaxial pressure: 10 tons, sintering time: 60 minutes, water additives: 25 wt%, Na_2CO_3 additives: 9 wt%) still demonstrate a relatively good effect in immobilizing cadmium. Additionally, within a certain range, the empirical model can be used to make predictions for the response variable with reasonable accuracy.

Table 8. Comparison of quality characteristics, S/N ratio calculated values, and experimental values for the optimal CSP conditions.

Cd	Additive Model Calculation Value	Experimental Values
quality characteristic (mg/L)	0.687	0.772
S/N ratio (dB)	2.842	2.227

Triple replicate cold sintering experiments were conducted using the optimal CSP conditions for fly ash, and the resulting sintered blocks were subjected to TCLP testing, along with the original fly ash sample. The results are shown in Table 9. In this study, cadmium was used as an indicator for the leaching concentration of heavy metals. The results indicate that under the optimal CSP conditions, there was a significant reduction in the leaching concentrations of cadmium (77.71%), lead (21.14%), zinc (42.37%), and chromium (99.99%) compared to the original fly ash sample. It is noteworthy that lead, zinc, and chromium, despite being heavy metals, exhibited different outcomes under the same solidification conditions. Based on the compositional analysis results in Table 3 and Table 4, it can be inferred that the high initial content of lead and zinc in the fly ash compared to cadmium and chromium may have exceeded the solidification limits of CSP or there might have been certain factors during the CSP process that hindered the effective solidification of lead and zinc.

Table 9. Comparison of TCLP results of CSP optimal conditions and FA sample.

	Cd	Pb	Zn	Cr
FA sample	3.239	2.663	31.915	0.589
CSP optimal condition	0.772	2.100	18.392	0.000

Preprints (www.preprints.org) | NOT PEER-REVIEWED | Posted: 8 August 2023 doi:10.20944/preprints202308.0203.v2

Percentage Increase/Decrease	-77.71%	-21.14%	-42.37%	-99.99%

Unit: mg/L.

3.4. Analysis of properties and solidification mechanism of fly ash CSP blocks

The fly ash ceramic blocks prepared under the optimal conditions of CSP at a temperature of 300°C, a uniaxel pressure of 10T, sintering time 60 minutes, water additives of 25 wt%, and a sodium carbonate (Na_2CO_3) addition of 9 wt% are shown in Figure 9, along with the XRD analysis results of the fly ash sample. The main phases identified in the fly ash include halite (NaCl, PDF#05-0628), quartz (SiO_2, PDF#46-1045), calcite ($CaCO_3$, PDF#05-0586), anhydrite ($CaSO_4$, PDF#37-1496), gypsum ($CaSO_4 \cdot 2H_2O$, PDF#33-0311), and sylvite (KCl, PDF#41-1476). During the CSP process, where multiple factors such as temperature, pressure, time, and liquid composition are simultaneously involved, the peak intensities of NaCl and KCl grad ually decrease, while new phases such as calcium silicate (Ca_2SiO_4, PDF#31-0302), rankinite ($Ca_3Si_2O_7$, PDF#22-0539), hydrogrossular ($Ca_3Al_2(SiO_4)_2(OH)_2$, PDF#420570), anorthite ($Ca(Al_2Si_2O_8)$, PDF#86-1716), and marilite ($(Na,Ca)_2(Si,Al)_6(O,OH)_{12}(Cl,CO3)_{0.5}$, PDF#31-1279) begin to appear. Based on the formation of secondary phases observed in Figure 9 and the effectiveness of heavy metal immobilization of fly ash under the optimal CSP conditions shown in Table 9, it can be inferred that the secondary phases generated during the CSP process have the ability to inhibit the leaching of internal heavy metals during the TCLP test to some extent.

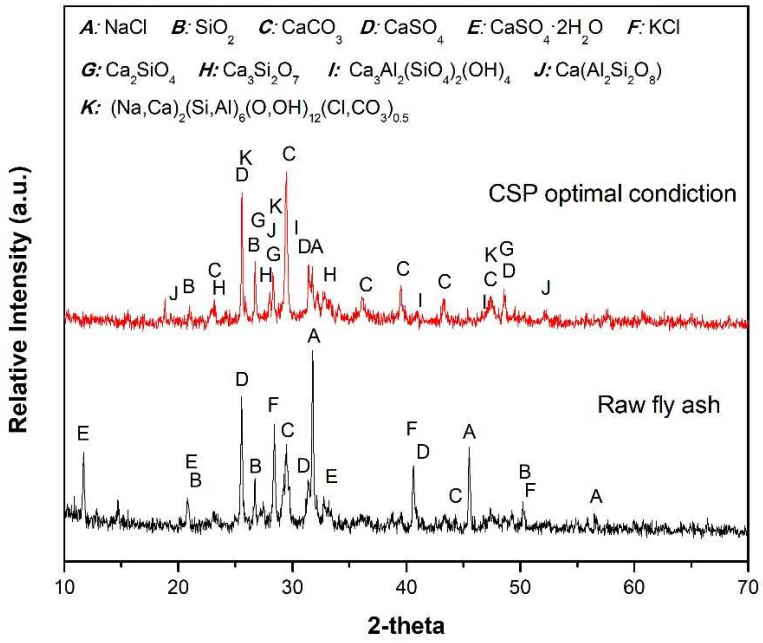

Figure 9. XRD diffraction results of fly ash sample and fly ash under optimal CSP conditions.

Under the combined influence of temperature, pressure, time, liquid composition, and sodium carbonate addition, the overall structure during the CSP process exhibits a high level of density. Figure 10(a) illustrates the sintered blocks of fly ash under the optimal CSP conditions, as observed by SEM at a magnification of 10,000 times. Compared to the untreated fly ash sample in Figure 6, the overall structure shows a significant improvement in density, with some small pores visible on the surface leading to the interior. From a CSP perspective, these small pores are likely remnants of water evaporating from the blocks at temperatures above the boiling point during the CSP. In Figure 11. (a) at the top left corner, it is evident that the fly ash ceramic blocks produced under the optimal CSP conditions display sharp fracture surfaces with distinct angular features. This indicates that the crystals possess specific growth directions during the crystallization process, indirectly supporting

Preprints (www.preprints.org) | NOT PEER-REVIEWED | Posted: 8 August 2023 doi:10.20944/preprints202308.0203.v2

the presence of secondary phases observed in the XRD results. Figure 11(b) reveals the intertwined growth patterns within the internal structure of the fly ash after undergoing the optimal CSP conditions. This suggests that when the fly ash sample is mixed with sodium carbonate and water, and subjected to the entire CSP process, reactions such as dissolution, precipitation, and the formation of new secondary phases occur between the fly ash particles. As a result, a dense and mutually enclosed structure is formed.

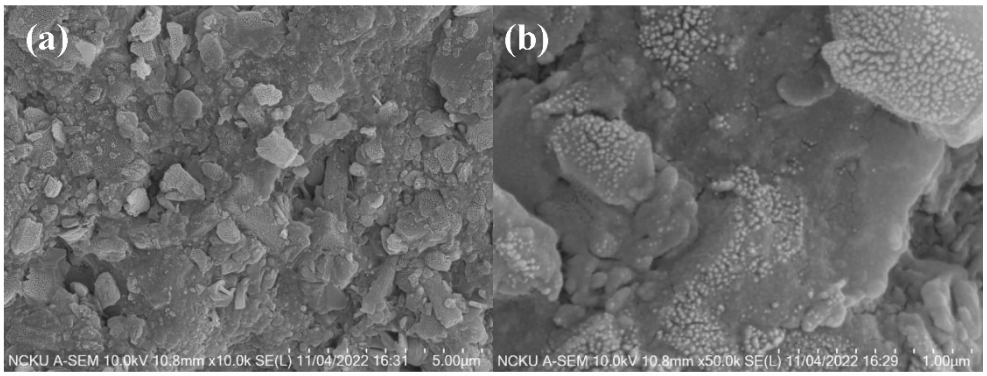

Figure 10. SEM image of optimal CSP condition fly ash blocks surface (a) 10,000x (b)50,000x.

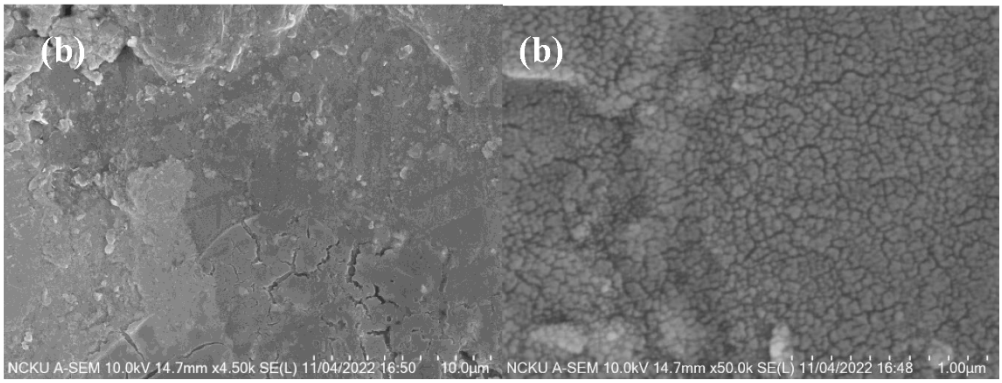

Figure 11. SEM image of optimal CSP condition fly ash bulk cross section (a) 4,500x (b)50,000x.

The SEM images captured in Figure 12 clearly reveal the presence of cavities at the bottom center of the image, which are formed when water escapes from the fly ash ceramic blocks under high temperatures and pressures. Upon examining the distribution of various elements on the surface of the blocks, it is evident that the concentrations of zinc and lead are relatively non-uniform, with significantly higher concentrations observed in the vicinity of the cavities at the bottom of the image. This suggests that during the CSP process, a portion of the lead and cadmium present in the fly ash dissolves in the added water. As the water gradually leaves the fly ash blocks under high temperature and pressure, these elements are transported to the surface of the blocks, resulting in poor solidification efficiency.

This phenomenon may be attributed to the fact that both zinc and lead are amphoteric metals. When the fly ash initially combines with water, the resulting solution exhibits strong alkalinity with a pH above 10. Consequently, lead, zinc, and other soluble substances are leached out together.

Figure 13 depicts the elemental distribution of zinc (Zn), lead (Pb), cadmium (Cd), and chromium (Cr) in the cross-section of the fly ash ceramic blocks under the optimal CSP conditions, as measured by EDS. In Figure 13, the SEM image, the distribution of zinc, lead, cadmium, and chromium elements appears to be more uniform compared to the surface of the blocks.

Preprints (www.preprints.org) | NOT PEER-REVIEWED | Posted: 8 August 2023 doi:10.20944/preprints202308.0203.v2

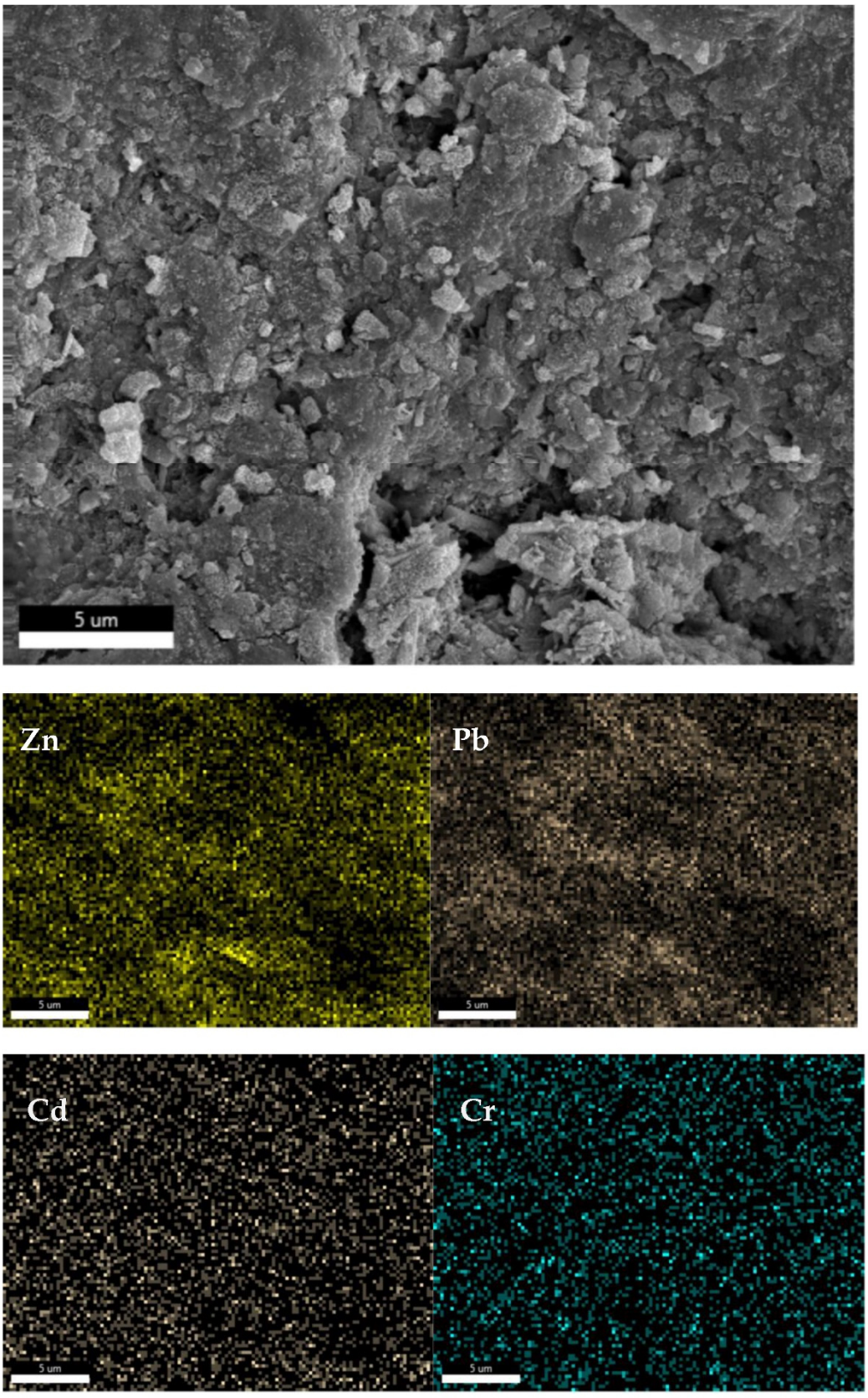

Figure 12. EDS analysis result of optimal CSP condition fly ash bulk surface.

Preprints (www.preprints.org) | NOT PEER-REVIEWED | Posted: 8 August 2023 doi:10.20944/preprints202308.0203.v2

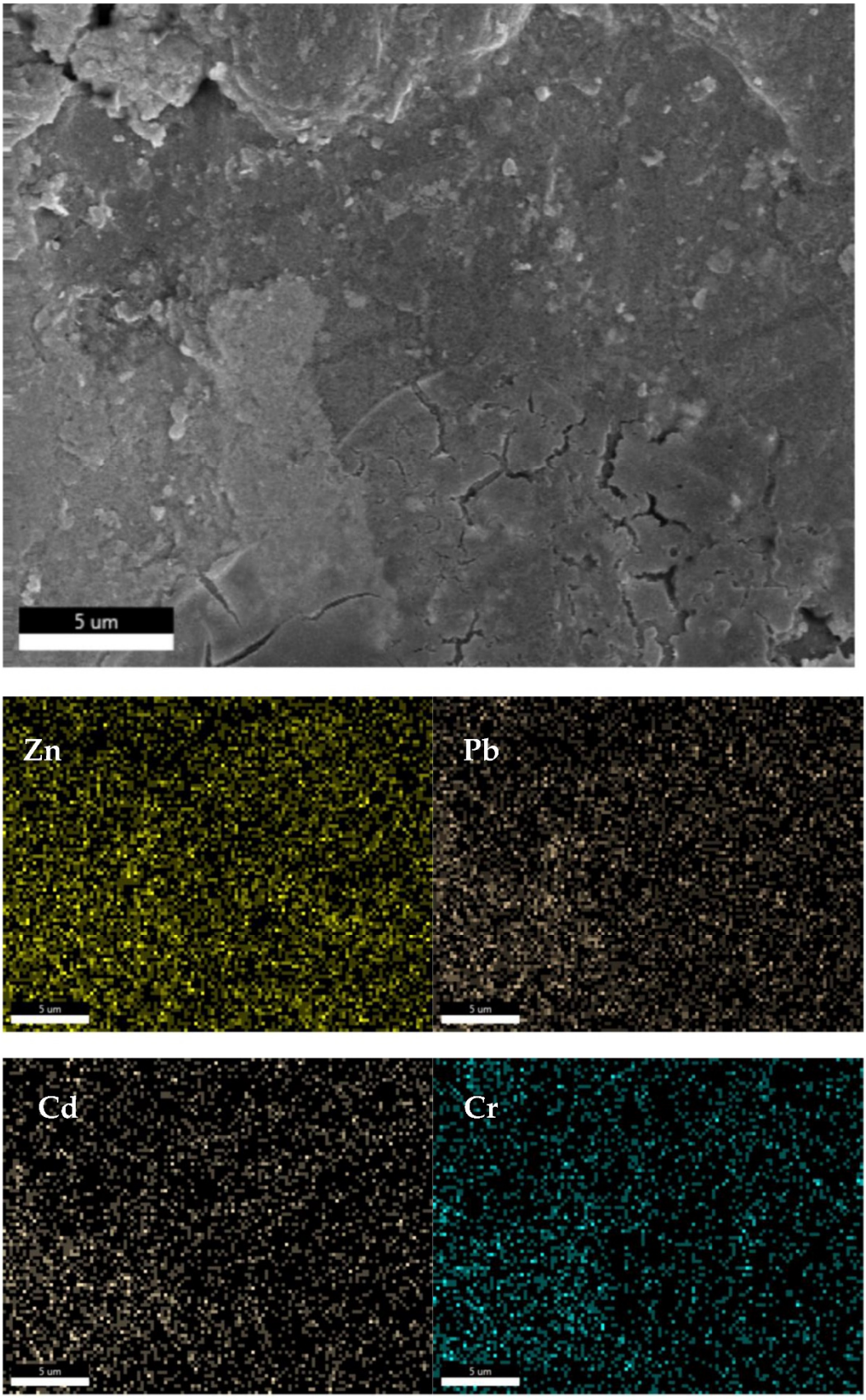

Figure 13. EDS analysis result of optimal CSP condition fly ash bulk cross section.

Based on the comprehensive analysis of XRD, SEM, and EDS results, the mechanism of internal heavy metal immobilization in fly ash through the CSP process is illustrated in Figure 14. Prior to CSP initiation, when pre-processed fly ash is mixed with sodium carbonate, water, and other

Preprints (www.preprints.org) | NOT PEER-REVIEWED | Posted: 8 August 2023 doi:10.20944/preprints202308.0203.v2

additives (Figure 1), certain substances on the surface of fly ash particles dissolve into the water, including some heavy metals. As CSP progresses, uniaxial stress is applied to the entire system, causing the fly ash particles to undergo mutual compression and plastic deformation, resulting in densification of the overall structure. Simultaneously, compared to the non-pressurized state, more surface substances of the fly ash particles dissolve. As the temperature increases, along with the applied uniaxial stress, more surface substances of the fly ash particles transfer to the liquid phase (resembling a pressurized leaching effect), where water plays a crucial role in mass transfer. As the temperature rises above the boiling point of water, water gradually evaporates from the interior of the blocks, leading to an increase in pH and the migration of some heavy metals from the interior to the surface of the blocks. Substances originally dissolved in the water (including heavy metals and soluble salts) become supersaturated due to water evaporation and precipitate between the fly ash particles. Simultaneously, under the influence of thermal and mechanical energy, phase transformations occur at the grain boundaries of the fly ash particles, resulting in the formation of stable secondary phases that encapsulate the precipitated heavy metals at the grain boundaries, thus reducing the leaching of heavy metals in the TCLP test. However, heavy metals carried to the surface of the blocks during the evaporation process are less effectively encapsulated by the newly formed secondary phases (such as lead and zinc) compared to those within the blocks, resulting in a lower immobilization effectiveness. This difference in effectiveness is also related to the higher content of lead and zinc in the fly ash, in addition to the nature of amphoteric metals.

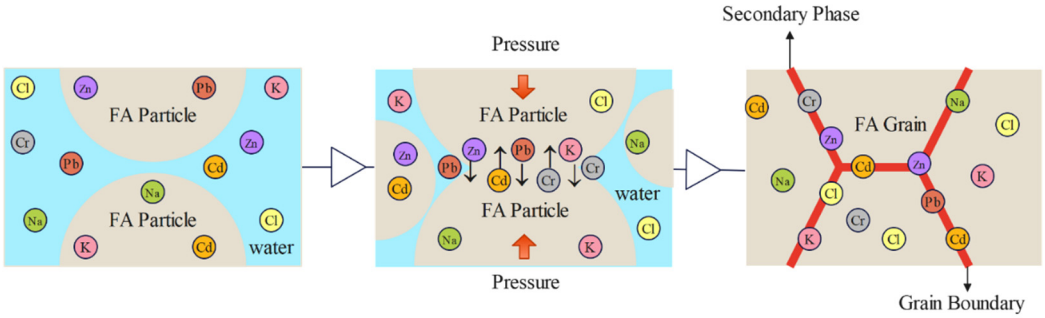

Figure 14. The schematic diagram illustrates the mechanism and process of heavy metal immobilization in fly ash through the CSP.

4. Conclusions

This study employed the cold sintering process (CSP) to effectively immobilize heavy metals present in fly ash by incorporating them into the subsequently formed secondary phases, such as Ca_2SiO_4, Ca_3Si2O_7, $Ca_3Al_2(SiO_4)_2$, and others. The CSP technique resulted in a significant reduction of the leaching concentrations of cadmium, lead, zinc, and chromium in fly ash by 77.71%, 21.14%, 42.37%, and 99.99%, respectively, thereby ensuring compliance with the TCLP regulatory limits.

To determine the optimal CSP conditions for minimizing the leaching of heavy metals, the Taguchi method was employed. The identified optimal conditions included a temperature of 300°C, pressure of 10T (312 MPa), time of 60 minutes, liquid ratio of 25 wt%, and sodium carbonate content of 9 wt%. These conditions facilitated effective heavy metal immobilization, particularly for cadmium and lead. Furthermore, the experimental model developed using the $L_{16}(4^5)$ orthogonal array was validated, revealing good predictability for cadmium leaching but some discrepancy for lead leaching. SEM-EDS analysis of the surface of CSP-treated fly ash blocks exhibited irregular particle morphology with distinct angular structures. Pore features were observed on the block surface, attributed to the evaporation of water during the CSP process. EDS analysis indicated significantly higher concentrations of lead and zinc in the vicinity of these pores, while no notable differences were observed for cadmium and chromium. The internal structure of the blocks displayed a spotted pattern, demonstrating a uniform distribution of elements.

Currently, the application of CSP for fly ash treatment is still in its early stages, but the results of this study demonstrate the potential of CSP technology in the future. Further research can explore

Preprints (www.preprints.org) | NOT PEER-REVIEWED | Posted: 8 August 2023 doi:10.20944/preprints202308.0203.v2

the effectiveness of CSP from the perspective of lead and zinc immobilization, explore different additive ratios, or investigate the combination of CSP with washed fly ash. These avenues present promising directions for future studies. In conclusion, CSP technology opens up a new pathway for ceramic materials, and if its unique characteristics are effectively utilized, it holds great potential for the future development of fly ash and other waste materials in the realm of resource recycling.

Author Contributions: Conceptualization, S.-K.L. and Z.-E.W.; methodology, Z.-E.W. and Y.-H.S.; Data curation, Z.-E.W. and S.-K.L.; Formal analysis, Y.-H.S. and Z.-E.W; Supervision, Y.-H.S.; Validation, Z.-E.W. and S.-K.L.; Visualization, Z.-E.W. and Y.-H.S.; Writing - original draft, Z.-E.W. and S.-K.L; Writing - review & editing, Y.-H.S..

Funding: This research received no external funding.

Acknowledgments: We express our gratitude to Dr. Che-Hao Lin and the research team members from the College of Intelligent Semiconductor and Sustainable Manufacturing at National Cheng Kung University for their valuable assistance in SEM imaging. We also extend our thanks to Dr. Yu-Hsien Lee and the research team members from the Institute of Resource Engineering at National Cheng Kung University, as well as the Department of Earth Sciences, for their kind support in XRD analysis.

Conflicts of Interest: The authors declare no conflict of interest.

References

1. Giro-Paloma, J., J. Formosa, and J.M. Chimenos, *Granular material development applied in an experimental section for civil engineering purposes.* Applied Sciences, 2020. **10**(19): p. 6782.
2. De Boom, A. and M. Degrez, *Belgian MSWI fly ashes and APC residues: a characterisation study.* Waste management, 2012. **32**(6): p. 1163-1170.
3. Huang, B., et al., *Recent progress on the thermal treatment and resource utilization technologies of municipal waste incineration fly ash: A review.* Process Safety and Environmental Protection, 2022. **159**: p. 547-565.
4. Xu, L., et al., *Status and Development Trend of Harmless and Resourceful Disposal of Municipal Solid Waste Incineration Fly Ash.* Adv. Environ. Prot., 2017. **7**: p. 414-422.
5. Mangialardi, T., *Disposal of MSWI fly ash through a combined washing-immobilisation process.* Journal of Hazardous Materials, 2003. **98**(1-3): p. 225-240.
6. Chang, L., et al., *A review of the applications of ion floatation: wastewater treatment, mineral beneficiation and hydrometallurgy.* RSC Advances, 2019. **9**(35): p. 20226-20239.
7. Liu, Z., et al., *Ash fusion characteristics of bamboo, wood and coal.* Energy, 2018. **161**: p. 517-522.
8. Sharifikolouei, E., et al., *Vitrification of municipal solid waste incineration fly ash: An approach to find the successful batch compositions.* Ceramics International, 2021. **47**(6): p. 7738-7744.
9. Zhang, Z., et al., *Stabilization/solidification of municipal solid waste incineration fly ash via co-sintering with waste-derived vitrified amorphous slag.* Waste Management, 2016. **56**: p. 238-245.
10. Quina, M.J., J.C. Bordado, and R.M. Quinta-Ferreira, *Treatment and use of air pollution control residues from MSW incineration: An overview.* Waste Management, 2008. **28**(11): p. 2097-2121.
11. Quina, M.J., J.C. Bordado, and R.M. Quinta-Ferreira, *Chemical stabilization of air pollution control residues from municipal solid waste incineration.* Journal of Hazardous Materials, 2010. **179**(1-3): p. 382-392.
12. Chen, X., et al., *Chlorides removal and control through water-washing process on MSWI fly ash.* Procedia Environmental Sciences, 2016. **31**: p. 560-566.
13. Chen, W.-S., et al., *Removal of chloride from MSWI fly ash.* Journal of Hazardous Materials, 2012. **237-238**: p. 116-120.
14. Huang, K., et al., *Leaching behavior of heavy metals with hydrochloric acid from fly ash generated in municipal waste incineration plants.* Transactions of Nonferrous Metals Society of China, 2011. **21**(6): p. 1422-1427.
15. Chen, Z., et al., *Fate of heavy metals during co-disposal of municipal solid waste incineration fly ash and sewage sludge by hydrothermal coupling pyrolysis process.* Waste management, 2020. **109**: p. 28-37.
16. Nagib, S. and K. Inoue, *Recovery of lead and zinc from fly ash generated from municipal incineration*

Preprints (www.preprints.org) | NOT PEER-REVIEWED | Posted: 8 August 2023 doi:10.20944/preprints202308.0203.v2

plants by means of acid and/or alkaline leaching. Hydrometallurgy, 2000. **56**(3): p. 269-292.
17. Tong, L., et al., *Investigation of controlling factors on toxic metal leaching behavior in municipal solid wastes incineration fly ash.* Environmental Science and Pollution Research, 2019. **26**(28): p. 29316-29326.
18. Kang, D., et al., *Heavy-metal reduction and solidification in municipal solid waste incineration (MSWI) fly ash using water, NaOH, KOH, and NH4OH in combination with CO2 uptake procedure.* Chemical Engineering Journal, 2020. **380**: p. 122534.
19. Funahashi, S., et al., *Cold sintering and co-firing of a multilayer device with thermoelectric materials.* Journal of the American Ceramic Society, 2017. **100**(8): p. 3488-3496.
20. Guo, J., et al., *Cold sintering process: A new era for ceramic packaging and microwave device development.* Journal of the American Ceramic Society, 2017. **100**(2): p. 669-677.
21. Randall, C.A., et al., *Cold sintering ceramics and composites*. 2017, Google Patents.
22. Kang, X., et al., *Cold sintering with dimethyl sulfoxide solutions for metal oxides.* Journal of Materials Science, 2019. **54**(10): p. 7438-7446.
23. Grasso, S., et al., *A review of cold sintering processes.* Advances in Applied Ceramics, 2020. **119**(3): p. 115-143.
24. Vakifahmetoglu, C. and L. Karacasulu, *Cold sintering of ceramics and glasses: A review.* Current Opinion in Solid State and Materials Science, 2020. **24**(1): p. 100807.
25. Galotta, A. and V.M. Sglavo, *The cold sintering process: A review on processing features, densification mechanisms and perspectives.* Journal of the European Ceramic Society, 2021. **41**(16): p. 1-17.
26. Toraya, H., M. Yoshimura, and S. Somiya, *Hydrothermal Reaction-Sintering of Monoclinic HfO2.* Journal of the American Ceramic Society, 1982. **65**(9): p. c159-c160.
27. Somiya, S., *Hydrothermal reactions for materials science and engineering: an overview of research in Japan*. 2012.
28. Gutmanas, E.Y., A. Rabinkin, and M. Roitberg, *Cold sintering under high pressure.* Scripta Metallurgica, 1979. **13**(1): p. 11-15.
29. Gutmanas, E., et al., *Cold Sintered Stainless Steel--Chromium Oxide Composites.* Progress in Powder Metallurgy 1985., 1985. **41**: p. 631-640.
30. Sun, P. and H.-C. Wu, *Splitting tensile strength of fly ash activated by hydrothermal hot-pressing process.* Journal of materials in civil engineering, 2009. **21**(8): p. 356-361.
31. Vakifahmetoglu, C., et al., *Reactive Hydrothermal Liquid-Phase Densification (rHLPD) of Ceramics – A Study of the BaTiO3[TiO2] Composite System.* Journal of the American Ceramic Society, 2016. **99**(12): p. 3893-3901.
32. Shi, H.-S. and L.-L. Kan, *Leaching behavior of heavy metals from municipal solid wastes incineration (MSWI) fly ash used in concrete.* Journal of hazardous materials, 2009. **164**(2-3): p. 750-754.

Disclaimer/Publisher's Note: The statements, opinions and data contained in all publications are solely those of the individual author(s) and contributor(s) and not of MDPI and/or the editor(s). MDPI and/or the editor(s) disclaim responsibility for any injury to people or property resulting from any ideas, methods, instructions or products referred to in the content.